Shear wave velocity imaging of the Avignonet landslide (France) using ambient noise cross correlation

F. Renalier,[1] D. Jongmans,[1] M. Campillo,[1] and P.-Y. Bard[1]

Received 25 September 2009; revised 12 March 2010; accepted 27 April 2010; published 11 September 2010.

[1] The Avignonet landslide affects a 2 by 2 km area covered by clayey deposits. This paper presents the use of the seismic ambient noise cross-correlation technique to retrieve a 3-D model of the shear wave velocity of the area. Seismic ambient noise was recorded during 15 days at 13 stations located on the landslide. Cross correlations computed between the vertical components of all station pairs allow the retrieval of the Rayleigh wave Green's functions and the estimation of their group velocity dispersion curves in the 1.7–5 Hz frequency range. At frequencies lower than 1.5 Hz, the anisotropy of the wavefield strongly influences the apparent Rayleigh wave velocities. Moreover, the analysis of the convergence of the cross correlations shows that at frequencies higher than 5 Hz, the recording time length was not sufficient for the cross correlation to be stable. These 1.7–5 Hz passive group dispersion curves are complementary to the ones computed from shot signals in the 3–7 Hz frequency range. A tomographic inversion of the resulting 1.7–7 Hz Rayleigh wave group dispersion curves provides local group dispersion curves at each cell of the tomographic grid. These are inverted with a neighborhood algorithm to retrieve the 3-D model of the landslide. Despite the complex wave propagation in the eastern part of the landslide and the sparse ray coverage, estimated velocities and first-order features are in good agreement with previous investigations.

Citation: Renalier, F., D. Jongmans, M. Campillo, and P.-Y. Bard (2010), Shear wave velocity imaging of the Avignonet landslide (France) using ambient noise cross correlation, *J. Geophys. Res.*, *115*, F03032, doi:10.1029/2009JF001538.

1. Introduction

[2] The Avignonet landslide is located in the Trièves area, 40 km south of the city of Grenoble (France) in the Western Alps (Figures 1a and 1b). This area is a large depression of about 300 km^2 covered by up to 200 m of Quaternary clays deposited during the Würm period in a glacially dammed lake. The erosion due to the Drac River and its tributaries since the melting of the glaciers has triggered numerous deep landslides along the river sides, and 15% of the clay cover is currently considered to be sliding [*Jongmans et al.*, 2009]. Most of these slides are moving slowly at a rate of a few cm/yr or less, but they might evolve into mudflows with dramatic acceleration. Such landslide sudden ruptures unfortunately occurred in l'Harmalière in 1981 [*Moulin and Robert*, 2004] and in La Salle en Beaumont in 1994 [*Moulin and Chapeau*, 2004], where four people were killed and nine houses and the church of the village were destroyed or seriously damaged. The geological and geotechnical properties of the glaciolacustrine clays outcropping in the Trièves area were intensively studied in the 1980s and summarized after more than 10 years of observations and geotechnical monitoring of several landslides [*Giraud et al.*, 1991; *van Asch et al.*, 1996]. These clayey deposits rest either on the Jurassic bedrock, faulted and folded during the Alpine orogenesis, or on highly compacted and cemented glaciofluvial materials (gravels and sands) deposited in paleovalleys of the Drac River during the interglacial Riss-Würm period. As illustrated in Figure 1c, the depth of the interface between clays and compact underlying units varies strongly laterally.

[3] A series of landslides affect the western side of the Monteynard Lake, which was created in 1962 by a dam built in the Drac River. Among them, the Avignonet landslide affects a surface of about 1×10^6 m^2 at the northern limit of the very active Harmalière landslide. On the basis of the affected surface and the depth of the deepest sliding surface found in boreholes at 40 m, the affected volume was previously estimated to be 40×10^6 m^3 [*Jongmans et al.*, 2008]. *Jongmans et al.* [2009] presented a detailed study of the Avignonet landslide, combining geotechnical and geophysical investigations. Four boreholes (labeled T0–T3, see location in Figure 2) were drilled in the southern part of the landslide where a hamlet is settled. Table 1 synthesizes the depths of the detected slip surfaces and geological interfaces. The contact between the clay and the underlying glaciofluvial deposits was found at 14.5 m and 56 m in T2 and T1, respectively. On the contrary, T0 and T3 only encountered clay deposits, in agreement with the westward thickening of this formation (Figures 1d and 1e). Inclinometer data and geological logs revealed at least three

[1]Laboratoire de Géophysique Interne et Tectonophysique, Grenoble Universités, Grenoble, France.

0148-0227/10/2009JF001538

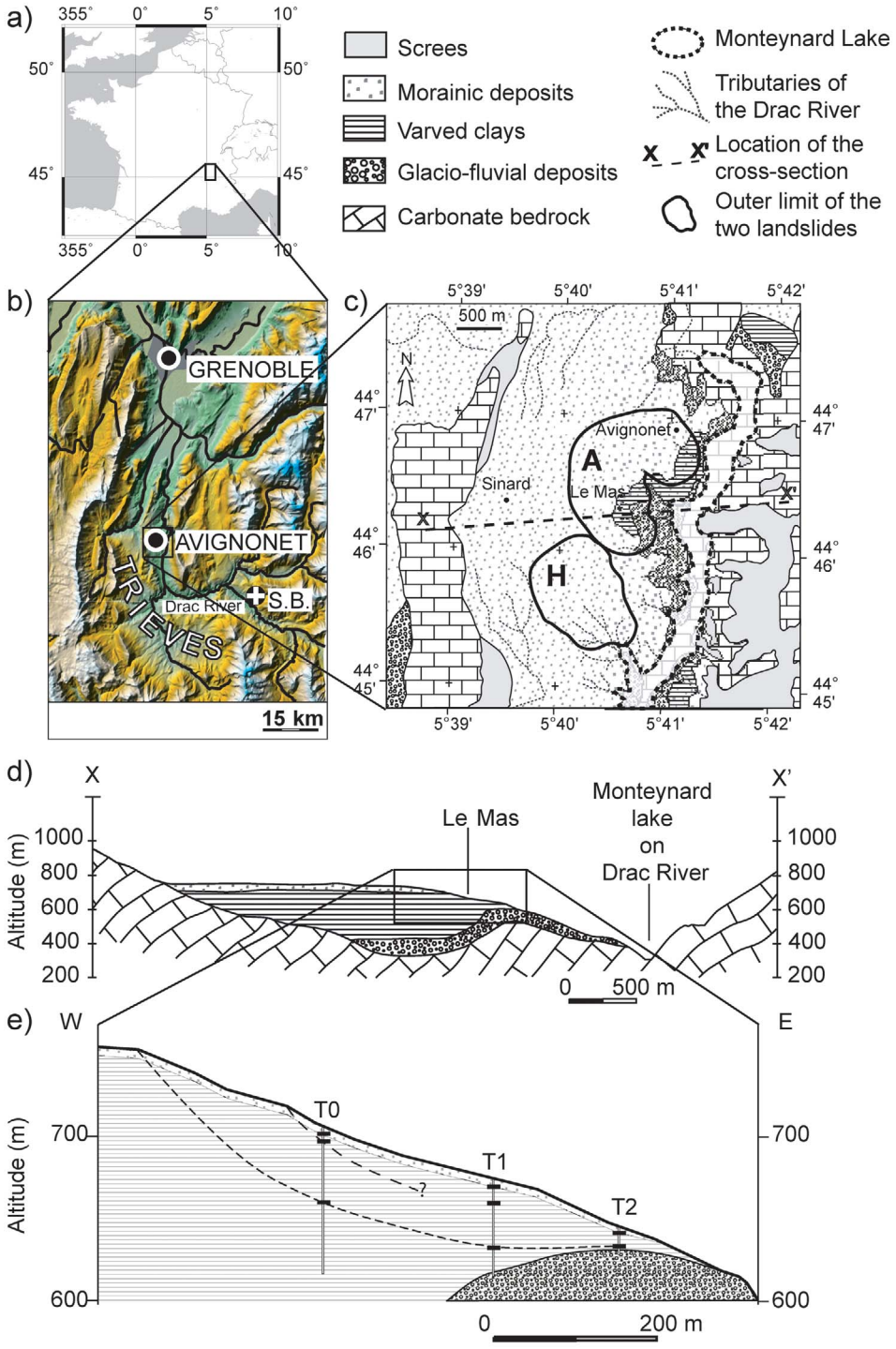

Figure 1. (a and b) Location of the Avignonet landslide in France and in the Western Alps. White cross in Figure 1b: location of La Salle en Beaumont. (c) Geological map of the Avignonet area. Thick black lines surround the Avignonet (A) and the Harmalière (H) landslides. Modified after *Jongmans et al.* [2009]. (d) Geological cross section indicated in Figure 1c. (e) Geological cross section of the Avignonet landslide with location of boreholes T0, T1, and T2 and position of observed slip surfaces. Modified after *Jongmans et al.* [2009].

rupture surfaces: a superficial one at a few meters depth, an intermediate one at 10–16 m, and a deep one at 42–47 m. Finally, a 17 m deep downhole test performed with a 1 m depth interval in a very disturbed area (close to borehole T3) showed that shear wave velocity (V_s) increases with depth, from less than 200 m/s at the surface to 400 m/s at the bottom, with velocity jumps that fit the rupture lines found at about 5 m and 14.5 m [*Bièvre et al.*, 2010]. *Jongmans*

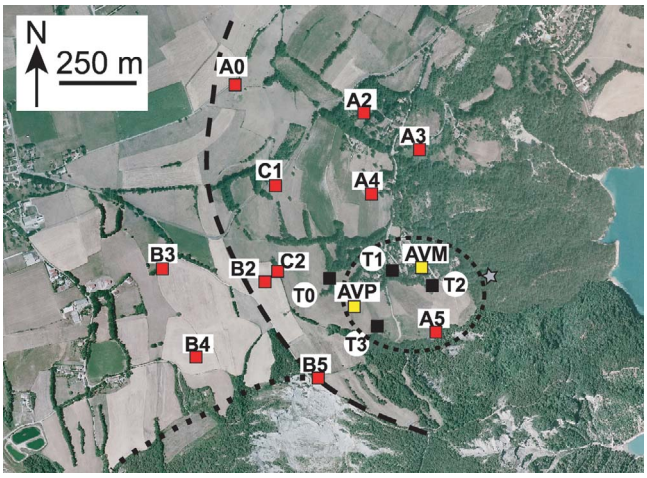

Figure 2. Acquisition layout on the landslide with 11 stations of the HRI network (red squares) and two permanent stations AVP and AVM (yellow squares). Dashed line is the outer limit of the Avignonet landslide. Dotted line is the limit of the Harmalière landslide. Dashed ellipse is the most active part of the landslide. Black squares show the locations of the four boreholes T0–T3 mentioned in section 6. Gray star shows the location of the outcrop of the glaciofluvial deposits.

et al. [2009] showed that the average slide velocity at the surface, measured by GPS during more than 10 years, increases downslope, varying from 0 to 2 cm/yr at the top, to more than 14 cm/yr at the toe. In parallel, they measured V_s at 5 m depth with active seismic experiments (refraction and surface wave inversion). They found that this parameter decreases from 500 m/s out of the landslide area to less than 200 m/s in the most disturbed zones. Their study enlightens the correlation between superficial displacement rates (related to clay deformation) and shear wave velocity on landslides affecting clayey deposits. Because V_s controls wave amplification [*Bard*, 1998], this correlation plays a great role in landslide self-excitation processes. For example, *Bozzano et al.* [2008] showed that the stabilized Salcito landslide (Italy) was reactivated in 2002 by the Molise earthquake because the landslide mass generated important amplification effects at frequencies consistent with its sliding mechanism and with the frequency spectrum of the earthquake. On the contrary, resistivity and *P* wave velocity images exhibited very little variations at depth and were found to be mostly controlled by the shallow water level within the clays. Unlike in other geological contexts such as the one of the Ancona landslide (Italy), where *Stucchi and Mazzotti* [2009] used high-resolution *P* wave reflection for deriving the geometry of the deepest sliding surface, these two geophysical parameters cannot be used for imaging features linked to the landslide activity.

[4] V_s may thus be a key parameter for investigating landslides in clayey deposits and delineating their geometry. The aim of the present paper is to contribute to the investigation of the Avignonet landslide by deriving a 3-D V_s model of its southern part.

[5] Shear wave velocity values are usually in situ measured by using various invasive (borehole tests) or noninvasive (shear wave refraction and reflection studies, surface wave inversion) techniques. Borehole tests have been extensively used in geotechnical engineering to a depth of a few tens of meters [e.g., *Pradel et al.*, 2005; *Schepers et al.*, 2001]. These techniques provide accurate and well-resolved V_s values, with the following drawbacks: (1) invasiveness, (2) increasing expense with depth, and (3) obtainment of only point estimates.

[6] Surface seismic tests provide shear wave velocities at lower cost (for reviews, see *Hack* [2000] and *Jongmans and Garambois* [2007]). They are based on the interpretation of body (shear transverse (*SH*)) or surface (Rayleigh or Love) waves. Techniques involving body waves include *SH* classical refraction, *SH* refraction tomography, and *SH* reflection studies. They are usually acquired on seismic profiles and require the active generation of waves with hammer and plate. However, the quality of *SH* seismic data can significantly be degraded by near-surface inhomogeneities [*Ata et al.*, 1993] and are therefore sometimes difficult to interpret in landslide areas, where the surface is disturbed.

[7] In recent years, surface wave methods have been increasingly used. The simplest one is the horizontal-to-vertical (H/V) technique [*Bard*, 1998], only requiring one three-component (3C) sensor to acquire the data. For sites with a strong impedance contrast, the frequency peak of the H/V ratio is related to the shear wave velocity and thickness of the top soft layer. If the thickness is known, V_s can be estimated and vice versa. More complex are the surface wave inversion techniques, which derive V_s as a function of depth in two steps: (1) estimating the surface wave dispersion curve from seismic records and (2) inverting this dispersion curve for the V_s profile (for a review, see *Socco and Jongmans* [2004]). Surface wave inversion methods are divided into two main categories on the basis of the kind of sources that generate the observed signals, i.e., active and passive methods. Active surface wave methods [*Park et al.*, 1999; *Eslick et al.*, 2008] (e.g., multichannel analysis of surface waves (MASW)) can be performed together with seismic *P* or *SH* refraction studies, provided the recording time length is long enough to contain the surface wave train. Passive surface wave methods use ambient vibrations or microtremors to retrieve the surface wave dispersion curve to lower frequencies than active techniques [*Aki*, 1957; *Satoh et al.*, 2001; *Okada*, 2003; *Nguyen et al.*, 2004]. However, surface wave dispersion curve inversion is based on the assumption that the underlying medium is not vary-

Table 1. Depths of the Three Sliding Surfaces and of the Interface Between Clays and Glaciofluvial Deposits in the Four Boreholes[a]

	Borehole Name			
	T0	T1	T2	T3
Depth of shallow slip surface (m)	5	–	1.5 and 4	5
Depth of intermediate slip surface (m)	10	15	12	10.3 and 14.5
Depth of deep slip surface (m)	47	43	–	42
Depth of contact between clays and glaciofluvial deposits (m)	–	56	14.5	–
Borehole depth (m)	89	59	17	49

[a]Borehole depths are also indicated.

ing laterally. Surface wave surveys have to be small enough not to break this assumption and therefore have a limited penetration depth [*Wathelet et al.*, 2008].

[8] *Jongmans et al.* [2009] applied these geophysical techniques to the Avignonet landslide; they performed *SH* refraction analysis on three 115 m long profiles and MASW on parts of a 480 m long profile, where wave propagation could be assumed to be 1-D. These techniques revealed V_s lateral variations but did not allow retrieving the deepest sliding surface found in boreholes at 40–50 m depth. Another method is thus needed for deriving a complete 3-D V_s model of the landslide at larger depth and for better reconstruction of the geometry of the landslide.

[9] At much larger scales, seismologists have also for a long time applied tomographic algorithms to derive global or regional 3-D models of the Earth by inverting volume or surface wave traveltimes measured on earthquakes recordings (for a description of these algorithms, see, for example, *Nolet* [2008]). These tomographies were limited by the quantity of earthquake data, which are not uniformly spread over the Earth and are sparse in time. To get around this limitation, it was recently proposed to use coda waves or long seismic noise records to retrieve the propagation characteristics between two receivers by cross correlation of the time series [*Campillo and Paul*, 2003; *Shapiro and Campillo*, 2004]. Actually, the use of the cross correlation function to retrieve the response between two points had been used in helioseismology [*Duvall et al.*, 1993] and in acoustics [*Weaver and Lobkis*, 2001]. Indeed, it has been demonstrated both theoretically and experimentally that the cross correlation of a diffuse wavefield recorded at two distant receivers converges toward the Green's function of the medium between these two receivers [*Sánchez-Sesma and Campillo*, 2006; *Gouédard et al.*, 2008]. This property was used at continental scale by *Shapiro et al.* [2005] for mapping the Rayleigh wave group velocity in California or by *Yao et al.* [2006] for deriving phase velocity images in SE Tibet. *Brenguier et al.* [2007] applied the same cross-correlation technique to the Piton de la Fournaise volcano (15 by 15 km) to retrieve Green's functions between all pairs of seismic stations; their dispersion curves, computed by frequency-time analysis, were inverted by tomography to retrieve group velocity maps for periods from 2 to 4.5 s. The local dispersion curves thus computed at all nodes of the tomographic grid were inverted to reconstruct a 3-D V_s image of the volcano, enlightening the chimney at its center.

[10] The objective of the present paper is to test the feasibility of the noise cross-correlation technique associated with surface wave tomography and dispersion curve inversion in estimating the 3-D shear wave velocity structure of the Avignonet landslide for a better assessment of its geometry. Section 2 reviews the cross-correlation technique and the underlying assumptions, keeping in mind its application to a kilometric-scale heterogeneous object such as the Avignonet landslide. Sections 3–5 detail the three steps of the process: (1) estimation of the Green's function by cross correlation, (2) estimation of dispersion curves by frequency-time analysis and tomography, and (3) dispersion curve inversion for the V_s model. Finally, we compare the results with previous studies performed on the landslide.

2. Green's Function Estimation From Cross Correlations

[11] The Green's function of a medium between two points A and B represents the wavefield recorded at A if an impulsive source is applied at B. In the case of an isotropic white noise, both experimental and theoretical studies showed that the cross correlation of the wavefields recorded at two points converges toward the (symmetric) Green's function between these points [*Weaver and Lobkis*, 2001; *Lobkis and Weaver*, 2001; *Derode et al.*, 2003a, 2003b; *Gouédard et al.*, 2008; *Colin de Verdière*, 2009]. *Sánchez-Sesma and Campillo* [2006] and *Sánchez-Sesma et al.* [2006] showed that for the problem of elastic waves, the convergence of noise cross correlation toward the Green's function is bonded by the equipartition condition of the different components of the wavefield. This condition can result from a uniform spatial distribution of noise sources [*Weaver and Lobkis*, 2001] or from infinite time averaging over a perfectly diffuse wavefield in a heterogeneous medium, scatterers acting as secondary sources [*Lobkis and Weaver*, 2001]. Neither of these two conditions are perfectly fulfilled in practical seismological experiments [*Campillo*, 2006], but most studies carried out until now showed that they compensate each other and allow at least a partial reconstruction of the Green's function [*Derode et al.*, 2003a, 2003b; *Larose et al.*, 2004; *Paul et al.*, 2005]. In these cases, the resulting signal may, however, not be symmetric.

[12] *Weaver and Lobkis* [2005] showed that for a medium with no attenuation where noise sources emit continuously, the amount of data needed to resolve a surface wave arrival (propagating in two dimensions) out of the fluctuations scales with the frequency and the distance between the receivers. However, they also pointed out that the signal-to-noise ratio obtained by *Campillo and Paul* [2003] for frequencies between 0.035 and 0.08 Hz was much lower than predicted by their calculations. They explained this discrepancy by the domination of local and uncorrelated noise sources in the noise records and by the absorption of the medium at these frequencies.

[13] To summarize, the convergence of the cross correlation toward the Green's function depends on the recording time length, on the isotropy of the wavefield (which depends on the position of noise sources and scatterers), on the frequency content of the noise sources, and on the frequency-dependent attenuation law of the medium.

[14] To our knowledge, only *Nunziata et al.* [2009] applied ambient noise cross correlation at kilometric scale and derived group velocity dispersion curves between several receivers deployed in the city of Naples (Italy). At this scale, targeted frequencies are above 1 Hz and are essentially generated by human activities [*Bonnefoy-Claudet et al.*, 2006]. Applying the cross-correlation technique for retrieving Green's functions on a landslide raises several questions. The first one regards the complexity of the medium itself: the landslide may in some places be too complex for the surface wave modes to even exist. This case was observed in active seismic data recorded on the Avignonet landslide [*Jongmans et al.*, 2009], where shots performed in a very active area were completely scattered by surrounding heterogeneities, preventing the application of any surface wave inversion on that particular area. The

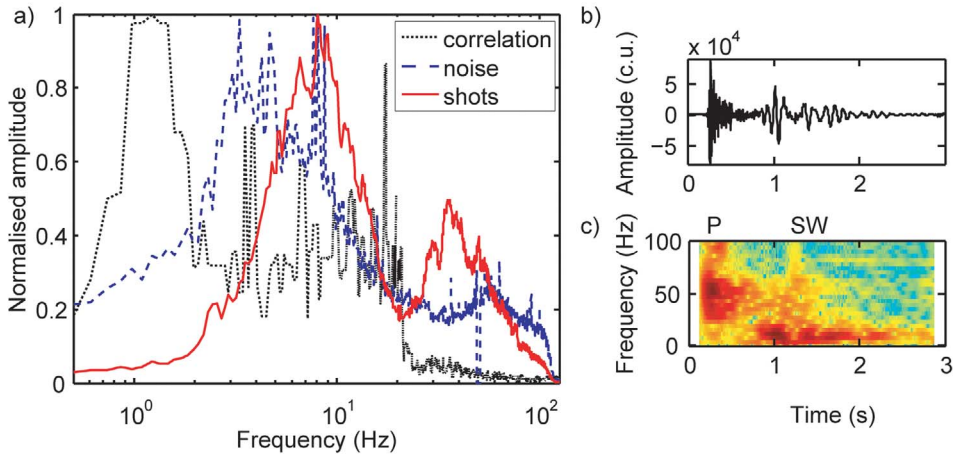

Figure 3. (a) Red line is the averaged normalized frequency content of all shot signals (vertical components). Dashed blue line is the averaged normalized frequency content of the vertical component of ten 1 h long noise records at all stations. The 50 Hz electricity peak was manually set to 0. Dotted black line is the average normalized frequency content of the cross-correlated signals (vertical component) between all station pairs (section 3.3). (b) Signal and (c) spectrogram of the shot at A0 recorded at A2 on the vertical component. P stands for *P* wave; SW stands for surface wave.

second question regards the rate of convergence and the related recording time length needed for the Green's function to emerge from cross correlations. For each frequency, this rate depends on the distance between receivers, on the presence of noise sources, and on the attenuation of the medium [*Larose et al.*, 2008]. Finally, the third question concerns the directivity of the noise wavefield at each frequency. These questions are addressed in section 3 before using the correlations for velocity estimation.

3. Green's Functions Estimation on the Avignonet Landslide

3.1. Data Acquisition and Recorded Signals

[15] Eleven stations of the High Resolution Imaging (HRI) network [*Coutant et al.*, 2008] were settled from 28 August to 12 September 2007 on the southern part of the Avignonet landslide, which is also equipped with two permanent stations named AVP and AVM (Figure 2). About two thirds of the sliding area were covered by this acquisition. The most active part of the landslide, in the southeastern part of the network (dashed ellipse in Figure 2), is the one that has been the most investigated previously. Seismic refraction profiles performed in the late 1950s by a private company (F. Blanchet, unpublished work, 1988) and the outcrop of the alluvium 200 m east of our array show that the compacted units underlying the glaciolacustrine clays are very close to the surface at this location (see Figure 1c). Moreover, the array also contains on its western part the outer limit of the landslide (dashed line), determined from geomorphological studies [*Kniess et al.*, 2009].

[16] All stations were connected to a 2–80 Hz 3C sensor, recording ambient noise continuously at a 250 Hz sampling rate. In order to assess the quality of the Green's functions computed from noise cross correlations, shots were performed with 200 g of explosive close to each 3C sensor. Most stations worked on the whole period, but B2 only recorded the first 3 days and C1, C2, and AVP only worked at the end of the period. AVM was unfortunately not working at that time, and the only available signals involving that station are the ones of the explosive shot performed close to the station.

[17] Figure 3a shows the frequency spectrum of both types of recorded signals: ambient noise (dashed blue line) and direct signals generated with explosive shots (red line). For ambient noise, the spectra of forty 1 h long signals recorded at each stations were averaged (all stations taken together) and then normalized. Apart from the 50 Hz electricity peak that was manually set to 0, this averaged spectrum shows one main frequency band between 1 and 15 Hz and some more energy between 50 and 70 Hz. The spectrum of direct shot signals, averaged from the spectra of all recorded shots, also shows two main frequency bands: between 3 and 20 Hz and between 25 and 60 Hz. This last frequency band corresponds to body waves, as illustrated in Figures 3b and 3c for the signal generated at A0 and recorded at A2 on the vertical component. In this paper, we concentrate on surface waves, computing the cross correlations in the 0.5–20 Hz frequency band.

3.2. Data Processing

[18] As previously experimented in several studies [*Stehly et al.*, 2007; *Brenguier et al.*, 2007], all 1 h long records were filtered between 0.5 and 20 Hz and their spectral amplitude was whitened in order to avoid dominance of strong spectral peaks in the noise. Moreover, only the sign of the signals was cross-correlated and the amplitude was disregarded so as not to overweight the most energetic events [*Campillo and Paul*, 2003; *Shapiro and Campillo*, 2004]. Finally, all correlations of 1 h records were stacked for each station pair.

3.3. Comparison With Direct Shots

[19] Figure 4 shows the comparison of the direct and cross-correlated signals involving station B3, filtered between 2 and 4 Hz. For direct signals (red line), negative

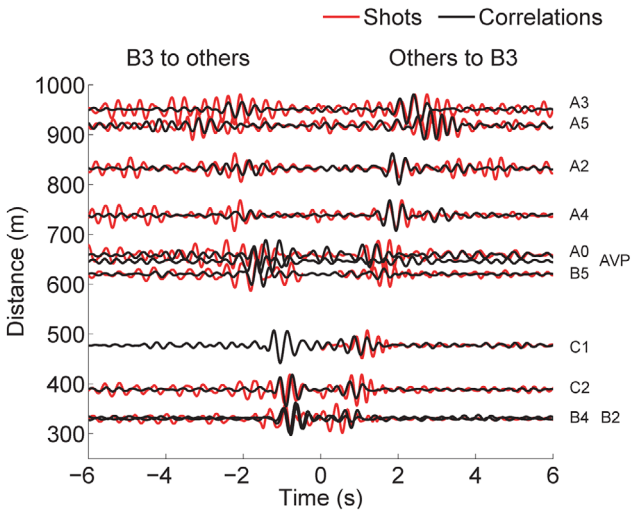

Figure 4. Comparison of the direct shot (red lines) and cross-correlated (black lines) signals between B3 and the other stations in the 2–4 Hz frequency band.

times correspond to the shot performed at B3 and recorded at all other stations, whereas positive times correspond to shots performed at all other stations and recorded at B3. For most paths, the arrival time and the phase of the main arrival are similar for both direct and cross-correlated signals, showing that the cross-correlation technique gives reliable results at these frequencies.

[20] The average spectrum of all cross-correlated signals is presented in Figure 3 together with the spectra of ambient noise and direct shots already discussed. As the ambient noise was band-passed and whitened between 0.5 and 20 Hz before cross correlation, the resulting cross-correlated signals do not contain any energy at frequencies higher than 20 Hz. The frequency peak around 1 Hz shows that the weak amount of energy present in the ambient noise is much more coherent than the more energetic noise at higher frequencies. We analyze further the different characteristics of these frequencies in sections 3.4 and 3.5.

3.4. Convergence of the Cross-Correlated Signals

[21] For studying the convergence of the cross correlations and determining whether sufficient time was recorded, we chose to adapt the method proposed by *Larose* [2005], which consists of comparing cross correlations computed for increasing correlated time lengths with a reference on the one hand and estimating the symmetry of the cross correlations on the other hand. The analysis was performed for frequencies f = 1, 3, 5, and 7 Hz. For each of them, the reference cross correlation was first computed by band-pass filtering the stacked cross correlation in the $f \pm 30\%$ frequency band. The correlated time length of this reference corresponds to the available record length (more than 250 h for most station pairs). Then, for increasing times of X h (X = 30, 60,…), X 1 h cross correlations are randomly chosen among all the available ones and stacked to obtain a partial cross correlation with a correlated time of approximatively X h. For each time, 20 different draws were performed, except for the longest times where there are less than 20 possible combinations. For each of these draws is computed the correlation coefficient between the partial and the reference cross correlation, both normalized by their respective maximum. The convergence of the cross correlations is determined from the average correlation coefficients computed at all different times. The analysis was performed separately on the causal and acausal parts of the cross correlations. Figure 5a represents such a study at 1 Hz for the path A0–B3 (660 m between stations). Negative (positive) correlated times correspond to the causal (acausal) part of the cross correlations, and the black lines correspond to the average trend on both of them. For this path and this frequency, correlation coefficients are very rapidly higher than 0.98, and the slope of the average trend is very close to 0 at long correlated times. The cross correlation is therefore stable, although this does not imply that it corresponds to the Green's function. All individual draws are represented by colored points, the color scale referring to the correlation coefficient between causal and acausal parts, also normalized by their maximum. This allows the estimation of the symmetry of the phase of the cross correlations. For this particular case (Figure 5a), all coefficients are between 0.9 and 1: the cross correlations are symmetric, which means that the same phases are reconstructed both ways.

[22] Figure 5b shows the same coefficients at 5 Hz for the same path A0–B3. The slope of the average trend at long correlated times is much steeper than in Figure 5a, and the cross correlations are not symmetric (blue). The averaging time was too short for the cross correlations to be stable and symmetric at this frequency and for this station pair. At the same frequency, the convergence is better achieved for shorter paths, as illustrated in Figure 5c for the path A2–A3 (230 m between stations). This enlightens the negative role of absorption in the convergence process.

[23] In order to evaluate globally the convergence of all computed cross correlations, we measured the slope of the average trend at long correlated times for all paths and each frequency. The corresponding histograms are plotted in Figures 5d–5g. At 1 and 3 Hz, this slope is less than 0.0002 at all station pairs, whereas at 5 and 7 Hz, some pairs present much steeper slopes. This indicates that at frequencies higher than 5 Hz, the cross correlations computed for some paths are not stable with the available record length and poorly reconstruct the Green's functions.

3.5. Location of Noise Sources

[24] The second point to check before deducing velocities from cross correlations regards the isotropy of the wavefield. For that purpose, all cross correlations are plotted in Figure 6, scaled by the distance between their receivers as a function of the back-azimuth of the receiver pair. If the wavefield is isotropic, the correct velocity will be reconstructed at all pairs. On the contrary, if energy comes from one preferential direction, in-line station pairs will give the right velocity, whereas perpendicular ones will show infinite velocity value (i.e., zero slowness). In Figure 6, black points correspond to the maxima of the envelopes of the cross correlations, i.e., to the apparent slowness of the reconstructed wave. At 1 Hz (Figure 6a), all maxima are aligned on a sine curve with maximum slowness for azimuths around 250°. One single source located to the west of the array dominates the wavefield at this frequency. It could correspond to the motorway that is running on the western

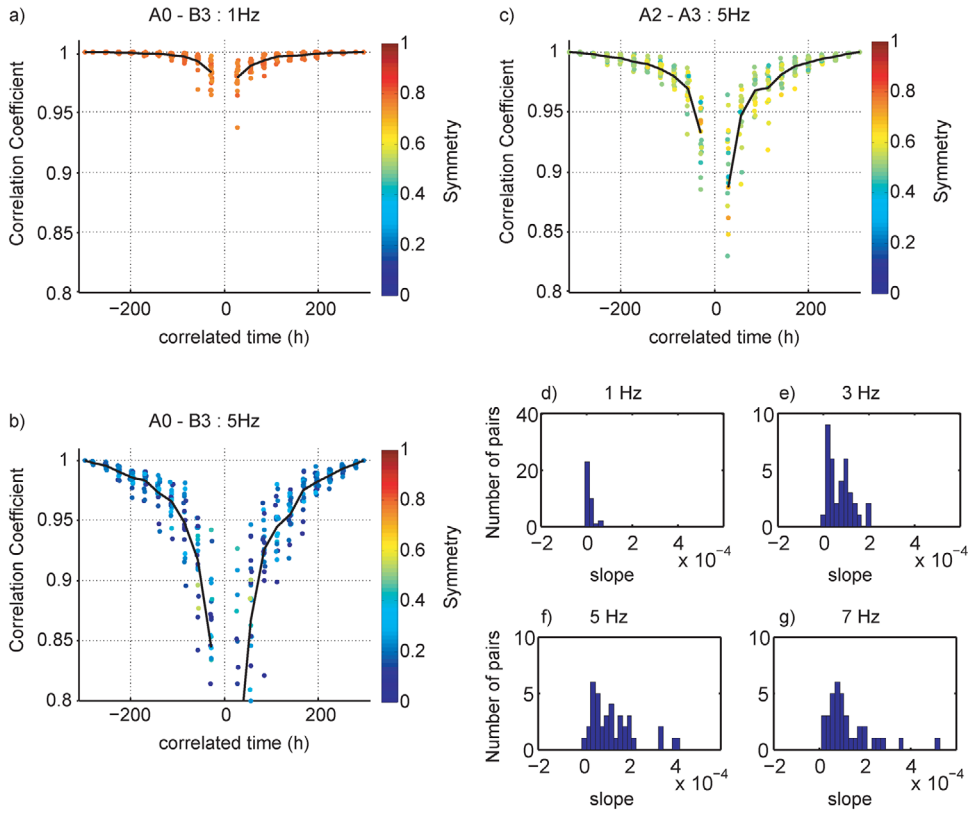

Figure 5. Convergence of the cross correlations with correlated time length. Evolution of the correlation coefficient between partial and reference correlations for both causal and acausal parts for (a) A0–B3 at 1 Hz, (b) A0–B3 at 5 Hz, and (c) A2–A5 at 5 Hz. Colors quantify the symmetry, i.e., indicate the correlation coefficient between causal (negative times) and acausal (positive times) parts for each particular draw. Black line is the average trend. (d–g) Histograms of the slopes of the average trend at long correlated times for all station pairs (between 200 and 260 h) at four different frequencies (1, 3, 5, and 7 Hz, respectively).

side of the plateau. Looking closer at the cross correlations, a second, less energetic sine curve symmetric to the first one is visible in Figure 6a. It is probably a reflection of the first one on the eastern edge of the plateau. At 2 Hz (Figure 6b), all maxima are, on the contrary, aligned on two parallel lines with roughly constant slowness. At this frequency like at higher frequencies (not shown), the wavefield is isotropic and velocities derived from stable cross correlations can be

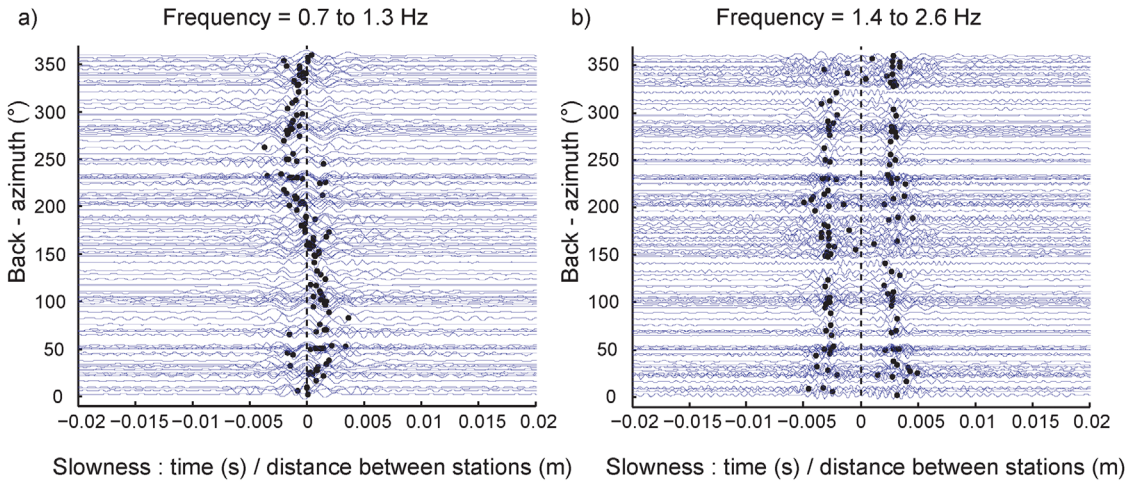

Figure 6. Cross correlations scaled by their interstation distance plotted versus the back-azimuth of the station pair and filtered between (a) 0.7 and 1.3 Hz and (b) 1.4 and 2.6 Hz. Black points correspond to the maximum of the envelope of the signals.

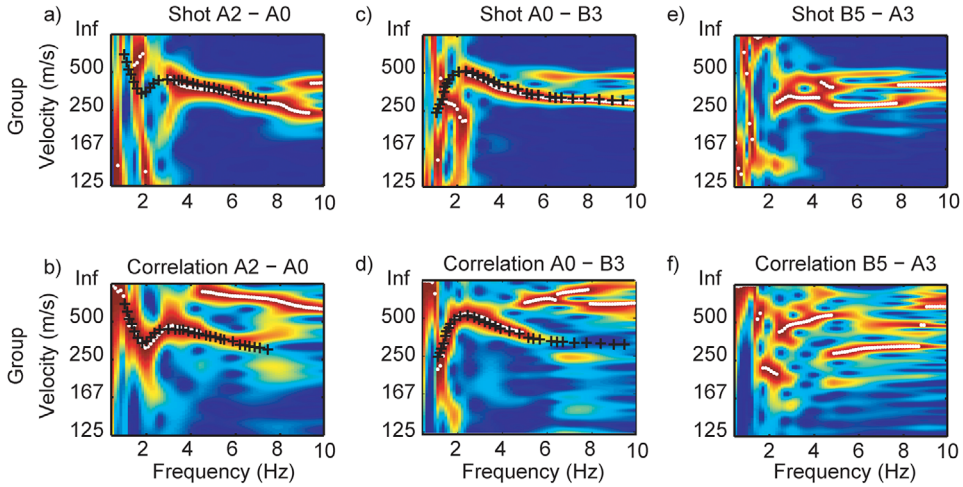

Figure 7. Rayleigh wave group velocity dispersion images computed on (a, c, and e) shots and (b, d, and f) cross-correlated signals for propagation from A2–A0 (Figures 7a and 7b), A0–B3 (Figures 7c and 7d), and B5–A3 (Figures 7e and 7f). Black crosses correspond to the picked velocity values for paths A2–A0 and A0–B3. No Rayleigh dispersion curve can be identified on the B5–A3 images, where the energy is completely split, certainly owing to the medium complexity.

interpreted with variations linked to the medium and not to wavefield characteristics. The next section thus presents such velocity measurements for frequencies higher than 1.5 Hz.

4. Surface Wave Dispersion

4.1. Dispersion Curves Identification

[25] Because computed cross correlations are not stable at high frequencies (section 3.4), active and cross-correlated signals were combined for estimating Rayleigh wave velocities on a wide frequency range. For each station pair, signals obtained for both directions of propagation were transformed to the time-frequency domain by using the *S* transform [*Stockwell et al.*, 1996]. In this frequency-time analysis technique, time window lengths are adapted to each frequency. Figure 7 presents the resulting group velocity dispersion images for the propagation from A2 to A0 (Figures 7a and 7b), from A0 to B3 (Figures 7c and 7d), and from B5 to A3 (Figures 7e and 7f) for active shots (Figures 7a, 7c, and 7e) and for cross correlations (Figures 7b, 7d, and 7f). The quality of the dispersion images is very variable from one pair of stations to the other. Generally, cross-correlated signals give valuable information for frequencies between 1.5 or 2 Hz to 3 to 6 Hz (Figures 7b and 7d), whereas explosive shot signals cover the 3–8 Hz frequency range (Figures 7a and 7c). At frequencies above 5–8 Hz, depending on the pair of stations, the fundamental mode of the Rayleigh wave cannot be identified, probably owing to the complexity of the wave propagation in the medium. Because of the very variable quality of the dispersion image (compare Figures 7a and 7c), dispersion curves were manually picked for each pair of stations (black crosses in Figures 7a–7d) when possible and take into account both directions and both active and cross-correlated signals. In total, 40–55 group velocity values were manually picked for each frequency between 1.5 and 7 Hz (by steps of 0.1 Hz). At higher frequencies, dispersion curves could only be identified on less than 40 paths. In order to keep a meaningful ray coverage, these data were not considered in the following inversions (sections 4.2 and 5.1). Moreover, on the basis of the overall comparison of the different dispersion curves available for each path, the uncertainty associated with these traveltime measurements was estimated to be approximatively 10% for the whole data set. By doing so, the same weight is given to all frequencies and paths in section 4.2.

4.2. Rayleigh Wave Tomography

[26] A tomographic inversion was performed on the arrival-time measurements deduced from the group velocity dispersion curves for frequencies between 1.5 and 7 Hz. Complex algorithms exist for performing such inversions, which use variable cell size for adapting the lateral resolution to the ray coverage [e.g., *Spakman and Bijwaard*, 2001] or run several iterations for optimizing ray paths [e.g., *Jobert and Jobert*, 1987]. However, the aim of the present work being mainly to test the feasibility of the method on a landslide and the data set being relatively small, we preferred to use the simple algorithm described by *Barmin et al.* [2001], which considers straight rays on a regular grid. In order to take into account the ray coverage, it includes a spatial smoothing term and a constraint on the amplitude of the perturbation depending on local path density. Because of the sparse ray coverage, we chose to give much importance to the spatial smoothing term [*Brenguier et al.*, 2007]. The tomographic grid involved 15 by 15 cells with 100 m sides, and we did not take into account the topography. This approximation induces errors smaller than 2%, whereas velocity variations are larger than 20% on all tomographic results (Figure 8). The uniform initial velocity model was computed at each frequency from the ratio of total distance to total time measured on all available rays. The computed group velocity maps are shown in Figure 8 for three frequencies (f = 1.7, 2.2, and 4 Hz). At low frequencies (1.7 Hz, Figure 8a), the eastern part is faster (up to 600 m/s) than the western one (around 300 m/s). At intermediate frequencies (2.2 Hz, Figure 8b), an area with low velocities (350 m/s)

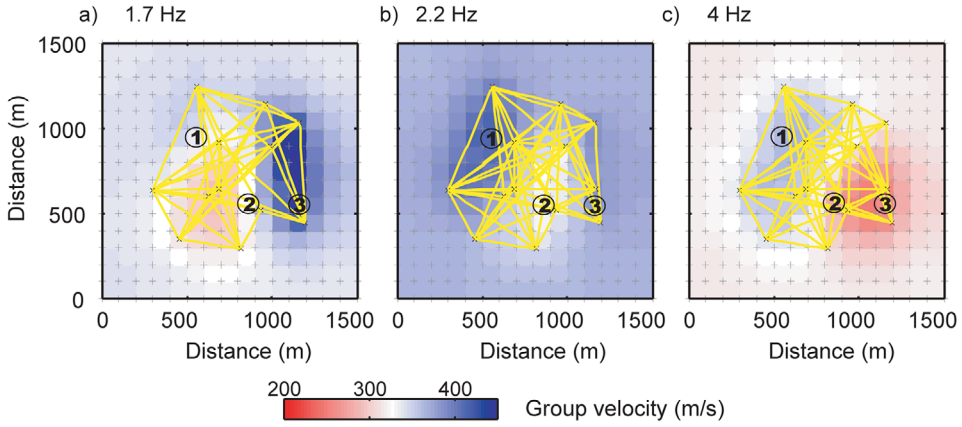

Figure 8. Rayleigh wave group velocity maps at (a) 1.7 Hz, (b) 2.2 Hz, and (c) 4 Hz. Numbers 1–3 refer to Figure 10.

is found in the south central part of the array. Finally, at high frequencies (4 Hz, Figure 8c), the southeastern part is slower (about 280 m/s) than the other parts of the model (around 350 m/s).

[27] In order to validate how well the anomalies at low and high frequencies are resolved, we performed two tests (Figure 9) with synthetic models presenting a high (low) velocity anomaly in the eastern (southeastern) part of the model for the ray coverages available at 1.7 Hz (4 Hz). Inversion of synthetic traveltimes (Figures 9c and 9d) shows that both anomalies are well reconstructed inside the array. However, their shapes are smoothed and their amplitudes are attenuated because of the strong smoothing term introduced in the tomographic inversion.

5. Inversion for the 3-D V_s Model

5.1. Inversion

[28] From the group velocity maps derived at all frequencies, local group velocity dispersion curves were reconstructed for each cell of the model. We used the neighborhood algorithm implemented in the Sesarray package [*Wathelet*, 2008] to invert these dispersion curves. As no significant low-velocity layer was found during previous investigations, the parameter space was a model with four uniform layers of increasing velocities with depth over a half space (Table 2). All V_p, V_s, Poisson's ratio (ν), and thickness values were inverted, but V_p and ν are poorly resolved and do not have any influence on the resulting V_s profiles (not shown). In the inversion, the fit between forward modeled and inverted dispersion curves was estimated through the misfit M:

$$M = \sqrt{\frac{1}{n}\sum_{i=1}^{n}\frac{(s_{\mathrm{m}_i} - s_{\mathrm{t}_i})^2}{s_{\mathrm{m}_i}^2}}, \qquad (1)$$

where s_{m} and s_{t} are the measured and theoretical group slownesses, respectively, and n is the number of frequencies.

[29] Figure 10 shows the results of such inversion for the cells 1–3 located in Figure 8. Cell 1 is representative of the western area, with low Rayleigh wave velocities at low frequencies (350 m/s at 1.7 Hz) and high velocities at intermediate and high frequencies (470 and 300 m/s at 3 and 6 Hz, respectively), relative to the other parts of the model. Cell 2 is representative of the south central part of the area, with low velocities at intermediate frequencies (320 m/s at 3 Hz), and cell 3 is representative of the southeastern part, with high velocities at low frequencies (450 m/s at 1.7 Hz) and low velocities at high frequencies (220 m/s at 6 Hz). Misfit values of the best inverted models are low on the whole grid, indicating that they explain correctly the data. For all cells, dispersion curves being limited at 7 Hz with

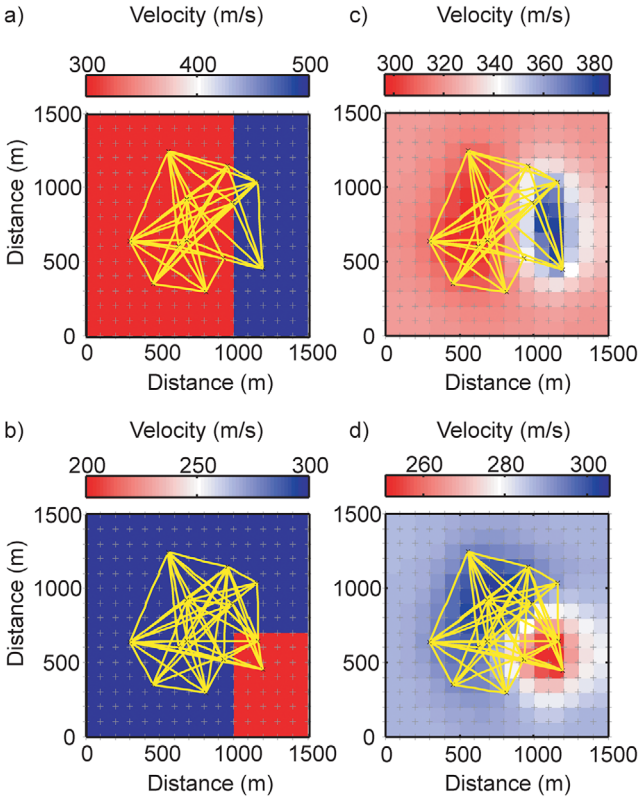

Figure 9. Spike tests. (a and b) Input models for the spike tests mimicking the tomographies at 1.7 and 4 Hz. (c and d) Corresponding inverted models.

Table 2. Parameter Space Used for the Dispersion Curve Inversion[a]

Layer	V_p	V_s	Bottom Depth	ν[b]	ρ[c]
1	200–5000	50–300	1–20	0.2–0.5	2000
2	200–5000	150–500	1–50	0.2–0.5	2000
3	200–5000	300–600	1–100	0.2–0.5	2000
4	200–5000	300–1000	1–250	0.2–0.5	2000
5 (bedrock)	200–5000	500–1200		0.2–0.5	2000

[a]No velocity decrease with depth is allowed.
[b]Here ν is Poisson's ratio.
[c]Here ρ is density.

velocities between 200 and 300 m/s, the first 10 m are not resolved by the inversion. V_s profiles in the western part of the array (cell 1, Figures 10a and 10d) show a velocity gradient down to about 50 m depth, over a thick uniform layer with V_s around 600 m/s, itself lying on a sharp interface ($V_s > 1000$ m/s) at a depth between 160 and 200 m. However, this depth corresponds to the penetration depth of our measurements, and we restrict the interpretation in section 5.2 to the upper part of the profiles. In the central part of the array (cell 2, Figures 10b and 10e), V_s profiles show a similar increase of velocity with depth down to 50 m. The underlying uniform layer has a slower velocity than in the western area (around 400–450 m/s). The profiles are not resolved below about 170 m depth; the bedrock here is not retrieved by the inversion. Finally, in the eastern part of the area (cell 3, Figures 10c and 10f), V_s profiles also exhibit a velocity gradient in the upper part, with velocities at about 15 m depth slower than in the other parts of the array (around 300 m/s versus 400 m/s in average elsewhere). Below this gradient, inversion results show a rather homogeneous unit with V_s between 500 and 800 m/s. However, this velocity is probably underestimated because of the poor ray coverage at low frequencies in this area and the smoothing applied in the tomography, as enlightened by the spike test in section 4.2 (Figures 9a and 9c).

5.2. 3-D V_s Model

[30] In order to construct a 3-D V_s model of the area, we computed for each cell the average of all V_s profiles that have a misfit lower than 1.2 times the minimum misfit. Figure 11 shows the reconstructed 3-D V_s model (Figure 11a) and two horizontal V_s maps at 15 and 60 m depth (Figures 11b and 11c, respectively). Note the significant vertical stretching of the z axis on the 3-D view and the difference in color scale between the 3-D view and the maps, which allows a better visualization of the different features. Moreover, the outer parts of the model are not resolved by the tomography and are therefore blurred.

[31] Five main features stand out, labeled A to E. Zone A, with high velocities below 150 m depth in the northwestern part of the model, probably corresponds to the bedrock stiff layers (alluvium and/or carbonate). As explained for the inversion of cell 1 (section 5.1), this part of the model lies beyond the penetration depth of our study, so it is not believed to be very reliable. Feature B is a low-velocity area ($V_s < 320$ m/s) close to the surface in the southeast of the area. It corresponds to the most active part of the landslide, also visible on the map at 15 m depth (Figure 11b). At this depth, velocities in undisturbed and disturbed clays (430 and 280 m/s, respectively) are in good agreement with previous

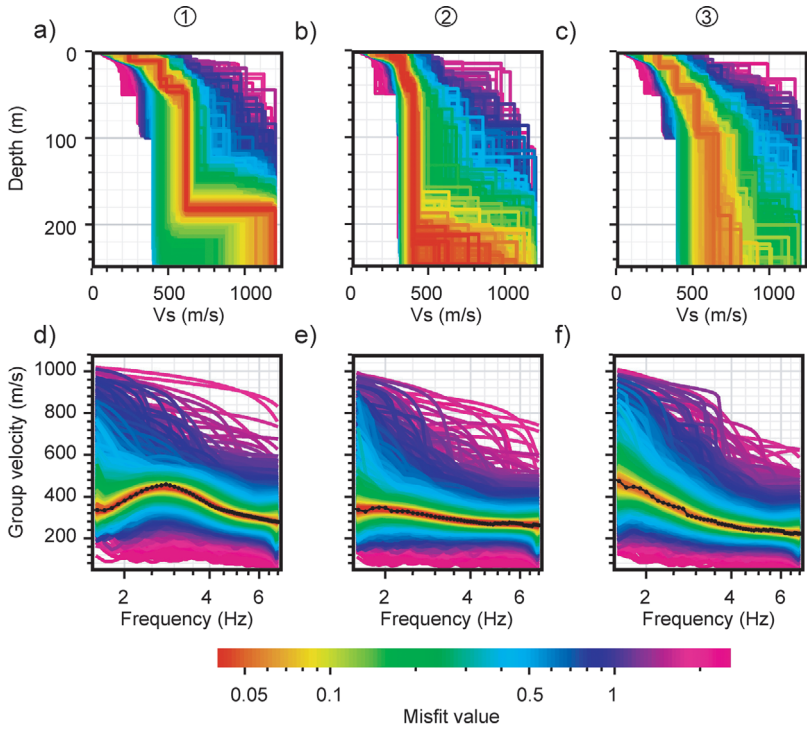

Figure 10. (a–c) V_s profiles resulting from the inversion of the local dispersion curves of cells 1–3 in Figure 8 with the parameter space described in Table 2. (d–f) Colors show the corresponding dispersion curves; black shows the inverted dispersion curves measured by tomography.

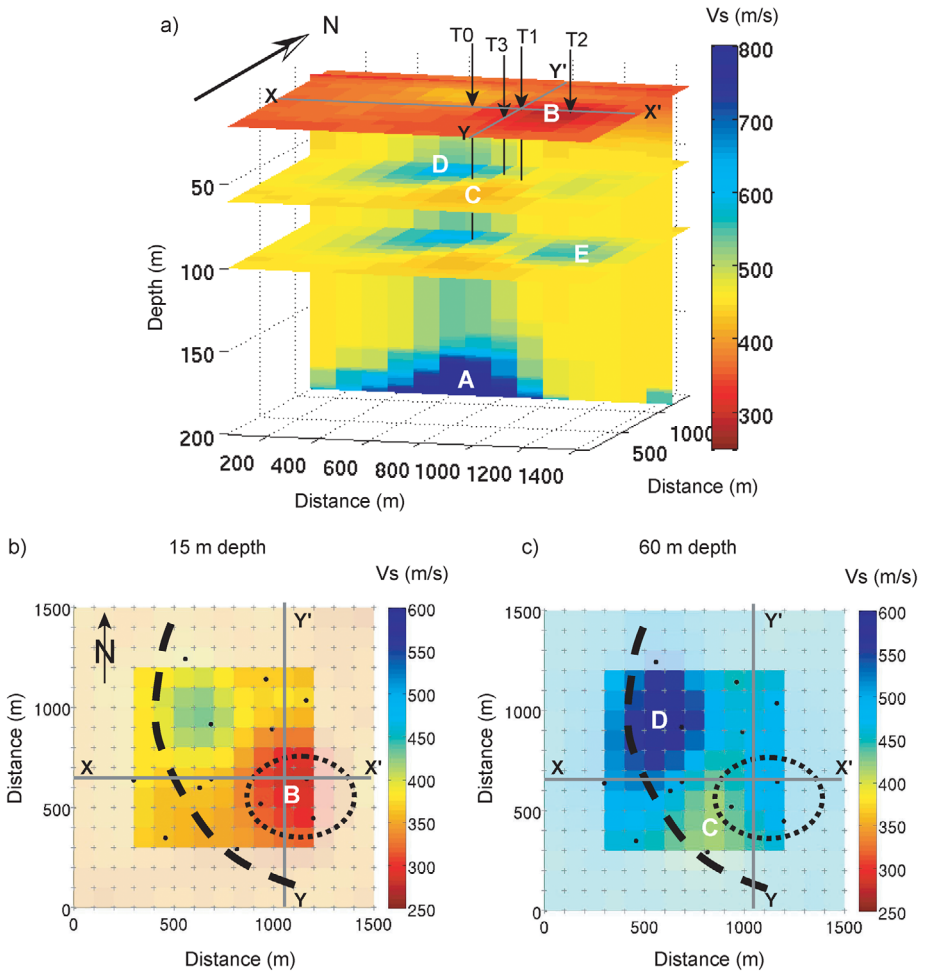

Figure 11. Three-dimensional V_s model resulting from the inversion. (a) Three-dimensional view from southeast, with horizontal slices at 15, 60, and 100 m depth. Arrows show the locations of boreholes T0–T3; A to E are particular areas described in text. (b and c) V_s maps at 15 and 60 m depth, respectively (with a velocity color scale different from Figure 11a). Dashed line is the outer limit of the landslide; dashed ellipse is the most active part of the landslide; and X-X' and Y-Y' are the positions of the sections presented in Figure 12.

studies: *Jongmans et al.* [2008] measured, respectively, 400 and 250 m/s at 10 m depth. Feature C is a deeper low-velocity area (420 m/s) in the south central part of the model, whereas zone D exhibits relative higher velocities (550–600 m/s). Both of them are visible on the map at 60 m depth. Low velocities of feature C are interpreted as being linked to the presence of the Harmalière landslide to the south (see Figures 1 and 2). Between 1981 and 2004, its head scarp has indeed continuously regressed by 10 m/yr [*Moulin and Robert*, 2004] and now intersects the Avignonet landslide limit. It is therefore likely that neighboring clays are already disturbed. On the contrary, high velocities of feature D (around 600 m/s) correspond to velocities usually encountered in the undisturbed clays of the area [*Jongmans et al.*, 2009]. Finally, feature E, with relatively high-velocity values (500–550 m/s) below the eastern part of the model, relates the shallow presence of the underlying bedrock. As mentioned earlier, these velocities are underestimated because of the smoothing applied in the tomographic inversion.

[32] In order to further compare our inverted model with previous studies, Figures 12a and 12b present two cross sections X-X' and Y-Y', whose location is shown in Figures 11b and 11c. The color scale is the same as used in the maps of Figure 11. Like the outer parts of the model, the upper 10 m are not well resolved (section 5.1) and were blurred. The west-east section X-X' (Figure 12a) crosses the head scarp of the landslide and intersects boreholes T0, T1, and T2. The south-north section Y-Y' (Figure 12b) passes through boreholes T1 and T3.

[33] The depths of the two slip surfaces observed in the four boreholes (Table 1), represented with crosses in Figures 12a and 12b, correlate very well with the two vertical velocity contrasts found in the inverted 3-D V_s model. First, a low-velocity unit (V_s < 320 m/s) lays on the internal slip surface observed at around 10 m depth in T1 and T2 (Figures 12a and 12b). Moreover, the landslide body as a whole is characterized by a slightly higher velocity (V_s < ~400 m/s) with a thickness of about 40 m below T0 and T1, which decreases to the west, in agreement with the location of the head scarp

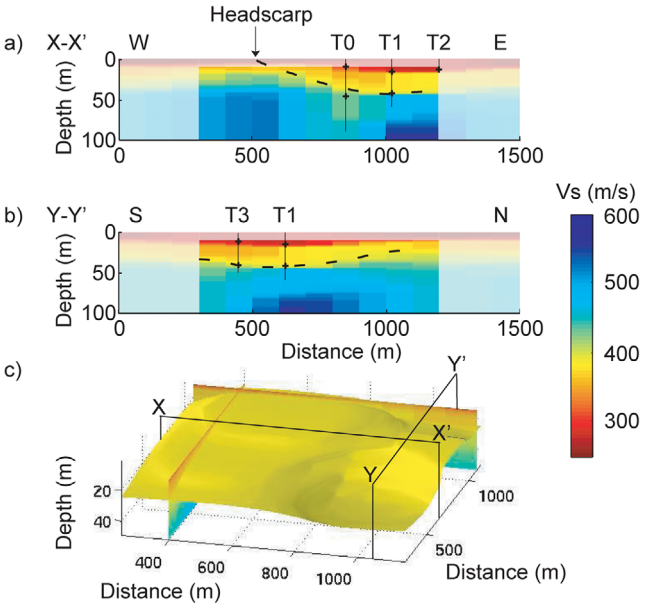

Figure 12. Comparison with previous investigations. Sections (a) *X*-*X*′ and (b) *Y*-*Y*′ down to 100 m. Their locations are given in Figure 12c. Crosses are depths of slip surfaces found in boreholes T0–T3; arrow shows the location of landslide head scarp; and dashed line is the interpreted deepest limit of the landslide. (c) Three-dimensional view of the 380 m/s isosurface, which approximately corresponds to the landslide deepest sliding surface.

(Figure 12a). The 380 m/s isosurface is plotted in Figure 12c, illustrating in the eastern part the shape of the deepest sliding surface. The 3-D V_s model shows that the landslide thickness decreases northward, from about 40 m depth to the south to about 25 m depth to the north of section *Y*-*Y*′ (Figure 12b). This suggests that the affected volume is smaller than previously thought. On the basis of the analysis of all sections across the model, we estimated the affected volume in the investigated area between 10 and 15 × 10^6 m^3. Extending the depth found at the northern edge of our model (25 m) to the last third of the landslide area to the north, the volume of clays affected by the Avignonet landslide in whole may be found in the order of 15–25 × 10^6 m^3.

[34] Each of the three processing steps induced uncertainties on the resulting model. First, no dispersion curves could be identified from the most complex waveforms, owing to the heterogeneity of the medium. This induced a simplification of the most irregular parts of the landslide. Moreover, most dispersion curves could only be identified up to 7 Hz, preventing imaging of the upper 10 m, where borehole measurements showed the shallowest sliding surface (Table 1). Laterally, the resolution is limited by the 100 m cell size and the strong smoothing constant used for tomography. Finally, the V_s profiles inverted from local dispersion curves depend on the adopted parameterization, which was chosen from a priori knowledge of the landslide.

6. Conclusions

[35] Seismic ambient noise cross correlation computed on a landslide affecting clayey deposits allowed the retrieval of the Rayleigh wave Green's functions and the estimation of their group velocity dispersion curves in the 2–5 Hz frequency range. These were complementary to the dispersion curves computed from shot signals in the 3–7 Hz frequency range. The analysis of the convergence of the correlations toward the Green's functions showed that at frequencies higher than 5 Hz, the recording time length was not sufficient for the cross correlation to be stable. This emphasizes the negative role of absorption in the convergence process. Looking at the azimuthal distribution of the retrieved slownesses, we observed a strong anisotropy of the wavefield at 1 Hz, dominated by waves from west to east and their reflection on the east of the area. Rayleigh wave dispersion curves were thus extracted between 1.5 and 7 Hz from the combination of active and passive measurements. Local group dispersion curves were computed in this frequency range by tomographic inversion. Because of the sparse ray coverage, we used a strong smoothing term, which allowed the correct imaging of soft lateral velocity variations but smoothed sharp contrasts such as the one in the southeast of the studied area (bedrock rise). The dispersion curves derived at all cells of the tomographic grid were inverted with a neighborhood algorithm for retrieving a 3-D V_s model of the area down to more than 100 m depth. The results are in very good agreement with previous investigations of the landslide.

[36] This work allowed a 3-D imaging of the Avignonet landslide and confirms that the cross-correlation technique may be applied for retrieving the Green's function on such kilometric size geological objects. The development of wireless acquisition systems such as the HRI network used in this study or the Wireless Array Analysis system [*Ohrnberger et al.*, 2006] should ease the acquisition of noise data at this scale. Regarding data processing, we needed here to combine correlations with active seismic data for extracting the high-frequency part of dispersion curves, and we were limited at low frequencies by the noise directivity. New processing techniques using, for example, time-frequency stacking algorithms based on the *S* transform [*Stockwell*, 2007; *Baig et al.*, 2009] should help to decrease the record length required at high frequencies. Moreover, the rotation algorithm proposed by *Roux* [2009] should allow the reconstruction of the Green's function even in the case of directional noise. Finally, joint inverting the Rayleigh wave dispersion curves with Love wave dispersion curves estimated from horizontal components and resonance frequencies derived from H/V ratios should help to constrain the inversion and to improve the resolution of the model at shallower and deeper depth, respectively [*Gouédard*, 2008; *Scherbaum et al.*, 2003]. The first application of the cross-correlation technique to a landslide is a promising result for imaging and monitoring kilometric-scale 2-D or 3-D objects.

[37] **Acknowledgments.** This work was funded by the European project NERIES and partly supported by the Mountain Risks Marie Curie project. The two permanent stations are part of the OMIV seismic network and are maintained by Rémi Béthoux, Catherine Péquegnat, and Ekaterina Bourova. We want to thank Yves Orengo, Fabrice Doré, and Sandrine Roussel for technical support during fieldwork, as well as three anonymous reviewers for their helpful suggestions, which improved the quality of the manuscript.

References

Aki, K. (1957), Space and time spectra of stationary stochastic waves, with special reference to microtremors, *Bull. Earthquake Res. Inst. Univ. Tokyo*, *35*, 415–456.

Ata, E., D. Corrigan, G. McMehan, and J. Gaiser (1993), Estimation of near-surface elastic parameters using multicomponent seismic data, *Geophysics*, *58*, 1017–1029.

Baig, A. M., M. Campillo, and F. Brenguier (2009), Denoising seismic noise cross correlations, *J. Geophys. Res.*, *114*, B08310, doi:10.1029/2008JB006085.

Bard, P.-Y. (1998), Microtremor measurements: A tool for site effect estimation?, paper presented at Second International Symposium on the Effects of Surface Geology on Seismic Motion, IASPEI/IAEE Joint Working Group on ESG, Yokohama, Japan.

Barmin, M. P., M. H. Ritzwoller, and A. L. Levshin (2001), A fast and reliable method for surface wave tomography, *Pure Appl. Geophys.*, *158*, 1351–1375.

Bièvre, G., F. Renalier, L. Valldosera, D. Jongmans, E. Flavigny, and P. Foray (2010), Caractéristiques de l'endommagement d'une argile par méthodes sismiques, paper presented at Journées Nationales de Géologie et Géotechnique, Com. Fr. de Geol. de l'Ingénieur et de l'Environnement, Grenoble, France.

Bonnefoy-Claudet, S., F. Cotton, and P.-Y. Bard (2006), The nature of the seismic noise wave field and its implication for site effects studies: A literature review, *Earth Sci. Rev.*, *79*(3–4), 205–227.

Bozzano, F., L. Lenti, S. Martino, A. Paciello, and G. Scarascia Mugnozza (2008), Self-excitation process due to local seismic amplification responsible for the reactivation of the Salcito landslide (Italy) on 31 October 2002, *J. Geophys. Res.*, *113*, B10312, doi:10.1029/2007JB005309.

Brenguier, F., N. M. Shapiro, M. Campillo, A. Nercessian, and V. Ferrazzini (2007), 3-D surface wave tomography of the Piton de la Fournaise volcano using seismic noise correlations, *Geophys. Res. Lett.*, *34*, L02305, doi:10.1029/2006GL028586.

Campillo, M. (2006), Phase and correlation in 'random' seismic fields and the reconstruction of the Green's function, *Pure Appl. Geophys.*, *163*, 475–502.

Campillo, M., and A. Paul (2003), Long-range correlations in the diffuse seismic coda, *Science*, *299*, 547–549.

Colin de Verdière, Y. (2009), Semi-classical analysis and passive imaging, *Nonlinearity*, *22*, R45–R75.

Coutant, O., F. Doré, F. Brenguier, J. Fels, D. Brunel, S. Judenherc, and M. Dietrich (2008), The High-Resolution Imaging (HRI) portable array: A seismic (and Internet) network dedicated to kilometric-scale seismic imaging, *Seismol. Res. Lett.*, *79*(1), 47–54.

Derode, A., E. Larose, M. Campillo, and M. Fink (2003a), How to estimate the Green's function of a heterogeneous medium between two passive sensors? Application to acoustic waves, *Appl. Phys. Lett.*, *83* (15), 3054–3056.

Derode, A., E. Larose, M. Tanter, J. de Rosny, A. Tourin, M. Campillo, and M. Fink (2003b), Recovering the Green's function from field-field correlation in an open medium (L), *J. Acoust. Soc. Am.*, *113*(6), 2973–2976.

Duvall, T., S. Jefferies, J. Harvey, and M. Pomerantz (1993), Time distance helioseismology, *Nature*, *362*, 430–432.

Eslick, R., G. Tsoflias, and D. Steeples (2008), Field investigation of Love waves in near-surface seismology, *Geophysics*, *73*(3), G1–G6.

Giraud, A., P. Antoine, T. van Asch, and J. Nieyuwenhuis (1991), Geotechnical problems caused by glaciolacustrine clays in the French Alps, *Eng. Geol.*, *31*, 185–195.

Gouédard, P. (2008), Techniques de corrélation: Aspects méthodologiques et applications à la sub-surface, Ph.D. thesis, Univ. Joseph Fourier, Grenoble, France.

Gouédard, P., et al. (2008), Cross-correlation of random fields: Mathematical approach and applications, *Geophys. Prospect.*, *56*, 375–393.

Hack, R. (2000), Geophysics for slope stablity, *Surv. Geophys.*, *21*, 423–448.

Jobert, N., and G. Jobert (1987), Ray tracing for surface waves, in *Seismic Tomography*, edited by G. Nolet, pp. 275–300, D. Reidel, Dordrecht, Netherlands.

Jongmans, D., and S. Garambois (2007), Geophysical investigation of landslides: A review, *Bull. Soc. Geol. Fr.*, *178*(2), 101–112, doi:10.2113/gssgfbull.178.2.101.

Jongmans, D., F. Renalier, U. Kniess, G. Bièvre, S. Schwartz, E. Pathier, Y. Orengo, T. Villemin, and C. Delacourt (2008), Characterization of the Avignonet landslide (French Alps) using seismic techniques, paper presented at 10th International Symposium on Landslides and Engineered Slopes, ISSMGE, Xi'an, China.

Jongmans, D., G. Bièvre, S. Schwartz, F. Renalier, N. Beaurez, and Y. Orengo (2009), Geophysical investigation of a large landslide in glaciolacustrine clays in the Trièves area (French Alps), *Eng. Geol.*, *109*, 45–56, doi:10.1016/j.enggeo.2008.10.005.

Kniess, U., D. Jongmans, E. Pathier, S. Schwartz, G. Bièvre, and T. Villemin (2009), Influence of bedrock topography on the kinematics of two clayey landslides in the Trièves (French Alps), paper presented at International Conference on Landslide Processes, Eur. Centre on Geomorphol. Hazards, Strasbourg, France.

Larose, E. (2005), Diffusion multiple des ondes sismiques et expériences analogiques en ultrasons, Ph.D. thesis, Univ, Joseph Fourier, Grenoble, France.

Larose, E., A. Derode, M. Campillo, and M. Fink (2004), Imaging from one-bit correlation of wide-band diffuse wavefield, *J. Appl. Phys.*, *95*, 8393–8399.

Larose, E., P. Roux, M. Campillo, and A. Derode (2008), Fluctuations of correlations and Green's function reconstruction: Role of scattering, *J. Appl. Phys.*, *103*, 114907.

Lobkis, O., and R. L. Weaver (2001), On the emergence of the Green's function in the correlations of a diffuse field, *J. Acoust. Soc. Am.*, *110* (6), 3011–3017.

Moulin, C., and C. Chapeau (2004), Le glissement de La Salle en Beaumont (Isère), paper presented at workshop Ryskhydrogeo, Program Interreg III, La Mure, France.

Moulin, C., and Y. Robert (2004), Le glissement de l'Harmalière sur la commune de Sinard, paper presented at workshop Ryskhydrogeo, Program Interreg III, La Mure, France.

Nguyen, F., G. van Rompaey, H. Teerlynck, M. van Camp, D. Jongmans, and T. Camelbeeck (2004), Use of microtremor measurement for assessing site effects in northern Belgium–Interpretation of the observed intensity during the *Ms* = 5.0 June 11 1938 earthquake, *J. Seismol.*, *8*, 41–56.

Nolet, G. (2008), *A Breviary of Seismic Tomography*, Cambridge Univ. Press, U. K.

Nunziata, C., G. D. Nisco, and G. Panza (2009), *S*-waves profiles from noise cross correlation at small scale, *Eng. Geol.*, *105*, 161–170.

Ohrnberger, M., D. Vollmer, and F. Scherbaum (2006), WARAN—A mobile wireless array analysis system for in-field ambient vibration dispersion curve estimation, paper presented at 1st European Conference on European Engineering and Seismology, ESC/EAEE, Geneva, Switzerland, 3–8 Sept.

Okada, H. (2003), *The Microtremor Survey Method*, translated from Japanese by K. Suto, *Geophy. Monogr. Series*, vol. 12, 135 pp., Soc. of Explor. Geophys., Tulsa, Okla.

Park, C., R. Miller, and J. Xia (1999), Multi-channel analysis of surface waves, *Geophysics*, *64*(3), 800–808.

Paul, A., M. Campillo, L. Margerin, E. Larose, and A. Derode (2005), Empirical synthesis of time-asymmetrical Green's functions from the correlation of coda waves, *J. Geophys. Res.*, *110*, B08302, doi:10.1029/2004JB003521.

Pradel, D., P. M. Smith, J. P. Stewart, and G. Raad (2005), Case history of landslide movement during the Northridge earthquake, *J. Geotech. Geoenviron. Eng.*, *131*(11), 1360–1369.

Roux, P. (2009), Passive seismic imaging with directive ambient noise: Application to surface waves and the San Andreas Fault in Parkfield, CA, *Geophys. J. Int.*, *179*, 367–373.

Sánchez-Sesma, F. J., and M. Campillo (2006), Retrieval of the Green's function from cross correlation: The canonical elastic problem, *Bull. Seismol. Soc. Am.*, *96*(3), 1182–1191.

Sánchez-Sesma, F. J., J. Pérez-Ruiz, M. Campillo, and F. Luzón (2006), Elastodynamic 2-D Green's function retrieval from cross-correlation: Canonical inclusion problem, *Geophys. Res. Lett.*, *33*, L13305, doi:10.1029/2006GL026454.

Satoh, T., H. Kawase, and S. Matsushima (2001), Estimation of *S*-wave velocity structures in and around the Sendai Basin, Japan, using array records of microtremors, *Bull. Seismol. Soc. Am.*, *91*, 206–218.

Schepers, R., G. Rafat, C. Gelbke, and B. Lehmann (2001), Application of borehole logging, core imaging and tomography to geotechnical exploration, *Int. J. Rock Mech. Min. Sci.*, *38*, 867–876.

Scherbaum, F., K.-G. Hinzen, and M. Ohrnberger (2003), Determination of shallow shear wave velocity profiles in the Cologne/Germany area using ambient vibrations, *Geophys. J. Int.*, *152*, 597–612.

Shapiro, N., and M. Campillo (2004), Emergence of broadband Rayleigh waves from correlations of the ambient seismic noise, *Geophys. Res. Lett.*, *31*, L07614, doi:10.1029/2004GL019491.

Shapiro, N., M. Campillo, L. Stehly, and M. Ritzwoller (2005), High-resolution surface wave tomography from ambient seismic noise, *Science*, *307*, 1615–1618.

Socco, L., and D. Jongmans (2004), Special issue on seismic surface waves, *Near Surface Geophys.*, *2*, 163–165.

Spakman, W., and H. Bijwaard (2001), Optimization of cell parameterizations for tomographic inverse problems, *Pure Appl. Geophys.*, *158*, 1401–1423.

Stehly, L., M. Campillo, and N. M. Shapiro (2007), Traveltime measurements from noise correlation: Stability and detection of instrumental time shifts, *Geophys. J. Int.*, *171*(1), 223–230.

Stockwell, R. (2007), A basis for efficient representation of the *S*-transform, *Digital Signal Process.*, *17*, 371–393.

Stockwell, R. G., L. Mansinha, and R. P. Lowe (1996), Localization of the complex spectrum: The *S* transform, *IEEE Transactions on Signal Processing*, *44*(4), 998–1001.

Stucchi, E., and A. Mazzotti (2009), 2D seismic exploration of the Ancona landslide (Adriatic Coast, Itay), *Geophysics*, *74*(5), B139–B151.

van Asch, T., M. Hendriks, R. Hessel, and F. Rappange (1996), Hydrological triggering conditions of landslides in varved clays in the French Alps, *Eng. Geol.*, *42*, 239–251.

Wathelet, M. (2008), An improved neighborhood algorithm: Parameter conditions and dynamic scaling, *Geophys. Res. Lett.*, *35*, L09301, doi:10.1029/2008GL033256.

Wathelet, M., D. Jongmans, M. Ohrnberger, and S. Bonnefoy-Claudet (2008), Array performances for ambient vibrations on a shallow structure and consequences over V_s inversion, *J. Seismol.*, *12*, 1–19.

Weaver, R., and O. Lobkis (2001), Ultrasonics without a source: Thermal fluctuation correlations at MHz frequencies, *Phys. Rev. Lett.*, *87*(13), 134301.

Weaver, R. L., and O. Lobkis (2005), Fluctuations in diffuse field-field correlations and the emergence of the Green's function in open systems, *J. Acoust. Soc. Am.*, *117*(6), 3432–3439.

Yao, H., R. Van Der Hilst, and M. de Hoop (2006), Surface-wave array tomography in SE Tibet from ambient seismic noise and two-station analysis: I–Phase velocity maps, *Geophys. J. Int.*, *166*, 732–744.

P.-Y. Bard, M. Campillo, D. Jongmans, and F. Renalier, Laboratoire de Géophysique Interne et Tectonophysique, Grenoble Universités, BP53, F-38041 Grenoble CEDEX 9, France. (denis.jongmans@obs.ujf-grenoble.fr)